Journal of
Materials Chemistry C

ROYAL SOCIETY
OF CHEMISTRY

PAPER

View Article Online
View Journal | View Issue

Check for updates

Cite this: *J. Mater. Chem. C*, 2021, **9**, 4771

Freestanding $CH_3NH_3PbBr_3$ single-crystal microwires for optoelectronic applications synthesized with a predefined lattice framework†

Shan-Shan Yan,[a] Yao Ma,[b] You-Chao Kong,[a] Ji-Zhong Jiang,[b] Xiu-Hua Xie,[ac] Shi-Chen Su,[de] Zi-Kang Tang,[a] Liang Shen,*[b] Shuang-Peng Wang*[a] and Kar Wei Ng*[a]

Received 23rd January 2021,
Accepted 4th March 2021

DOI: 10.1039/d1tc00316j

rsc.li/materials-c

Metal halide perovskites (MHPs) have shown unparalleled potential for optoelectronic applications. In particular, the quasi one-dimensional perovskite structures have attracted great attention due to their unique optoelectronic properties which can open up new possibilities for this exciting materials system. However, it is challenging to acquire one-dimensional cubic-phase MHPs in high yield due to their isotropic crystallization nature and instability towards conventional fabrication processes. Here, we demonstrate the feasibility of synthesizing single-crystalline perovskite microwires from an intrinsic 1D structured lattice framework which defines the size and shape of the resulting microwires. By incorporating the appropriate monovalent ions into the lattice of self-assembled $PbBr_2$ microwires, single-crystal $CH_3NH_3PbBr_3$ microwires are successfully synthesized. The excellent crystal quality of the microwires has led to a high carrier mobility of 36 $cm^2\ V^{-1}\ s^{-1}$ and a long charge carrier lifetime of $\sim$100 ns. As a preliminary demonstration of their optoelectronics functionality, single $CH_3NH_3PbBr_3$ microwire-based photodetectors are fabricated and the devices exhibit a fast response time (a rise time of 113 μs and a decay time of 295 μs), stable light switching behavior, high sensitivity, and good spatial resolution. The method described here proposes a novel and facile strategy for synthesizing single-crystal perovskite microwires with high yield and repeatability, showing the great promise of MHPs in micro-optoelectronic applications.

Introduction

Hybrid organic–inorganic halide perovskites (HOIPs) have attracted much attention for high performance optoelectronic applications due to their remarkable advantages, such as high quantum yield, high light absorption coefficient, long charge carrier diffusion length, and tunable direct bandgap.[1–7] Notably, the absorption coefficient of the perovskite in the visible wavelength range is much larger than that of most existing optoelectronic materials, resulting in a much higher photosensitivity which can be useful for photovoltaics and photodetection.[8] Indeed, remarkable progress has been achieved in the development of hybrid organic–inorganic perovskite solar cells (PSCs), with their power conversion efficiency (PCE) soaring from 3.8%[9] to 25.2%[10] over the past ten years. In addition to PSCs, HOIPs have also displayed great potential in many other optoelectronic fields such as in field effect transistors (FETs),[11,12] light-emitting diodes (LEDs)[13,14] and photodetectors.[15,16] Structural and morphological engineering has been the key to tailoring the optical and electrical properties of HOIPs so that they can fulfill the specific requirements of different applications.[17] In particular, stripe-like quasi-1D and 1D structures are favorable for realizing microlasers[18,19] and waveguides[20,21] due to their special geometry which allows efficient optical confinement. Moreover, in contrast to polycrystalline perovskite thin films, 1D structures usually have a high crystallinity which promises a longer lifetime of the photogenerated carriers, better charge separation and conductivity.[22,23] As such, great emphasis has been placed on the development of

---

[a] *Joint Key Laboratory of the Ministry of Education, Institute of Applied Physics and Materials Engineering, University of Macau, Avenida da Universidade, Taipa 999078, Macau, China. E-mail: spwang@um.edu.mo*

[b] *State Key Laboratory of Integrated Optoelectronics, College of Electronic Science and Engineering, Jilin University, Qianjin Street, Changchun 130012, People's Republic of China*

[c] *State Key Laboratory of Luminescence and Applications, Changchun Institute of Optics, Fine Mechanics and Physics, Chinese Academy of Sciences, No. 3888 Dongnanhu Road, Changchun, 130033, People's Republic of China*

[d] *Institute of Optoelectronic Material and Technology, South China Normal University, Guangzhou 510631, People's Republic of China*

[e] *SCNU Qingyuan Institute of Science and Technology Innovation Co., Ltd, Qingyuan 511517, China*

† Electronic supplementary information (ESI) available. See DOI: 10.1039/d1tc00316j

perovskite nano- and micro-wires, which show great potential in micro-optoelectronic applications.

Despite the many wonderful properties and potential applications, the synthesis of HOIP nano- and micro-wires remains challenging. The isotropic pseudo-cubic lattice of many perovskite materials intrinsically disfavors the growth of HOIP crystals naturally into anisotropic structures with high yield and controllability such that other structures like nanosheets and bulk crystals will also appear at the same growth.[24] And the instability of perovskite towards solvents commonly used in conventional semiconductor fabrication processes makes it hard to realize HOIP microwires *via* top-down approaches.[25] Template assisted anti-solvent growth has therefore been developed to realize 1D perovskite structures,[18,26,27] and has led to many excellent results in nanowire lasers and micro-/nano-wire array photodetectors. The use of templates, however, can undesirably introduce defects and impurities, while the well-designed templates definitely increases the complexity of the process.[28,29] Moreover, it has been difficult to transfer these nano/microwires, which are grown and fixed within confined regions, to other substrates for subsequent device fabrication.[30] In addition, these bottom-up growths are generally very sensitive to the crystal growth conditions, such as temperature, and precursor concentration disturbance. Precise control of these process parameters can be challenging and can lead to uncertainties in process repeatability. Hence, it is highly desirable to develop a novel growth strategy to obtain high quality transferable perovskite microwires with high yield and repeatability.

In this study, we demonstrate a facile method to realize size-controllable halide perovskite single-crystal microwires by synergizing the natural anisotropic growth of $PbBr_2$ single-crystals with the efficient incorporation of monovalent ions into the predefined lattices. Specifically, we synthesize single crystal $PbBr_2$ microwires as the initial framework, in a way which is distinctively different from the previous two-step methods in which mixed polycrystalline microstructures (including wires, plates, *etc.*) have been employed for conversion into perovskite.[31,32] Owing to its anisotropic orthorhombic crystal structure, $PbBr_2$ can be grown naturally into wires with lengths adjustable from the microscale to the centimeter scale *via* a spontaneous self-assembled process which shows high yield and repeatability. The $PbBr_2$ single crystals, having the desired size and shape, then act as a lattice framework for the formation of perovskite microwires by allowing the appropriate monovalent ions (*e.g.* $CH_3NH_3^+$ (MA^+) ions) to diffuse into the lattice, thus converting the binary compound into perovskite microwires. In contrast to the template-assisted growth, our synthesis method does not require the use of any mask which can introduce impurities or defects into the perovskite lattice. It is worth noting that the freestanding $PbBr_2$ microwires have been obtained in solution and can be easily transferred to various substrates for device fabrication.[33] $CH_3NH_3PbBr_3$ microwires with high crystallinity and purity can therefore be realized with high yield and repeatability using the simple solution-based processes. Indeed, extensive material characterization reveals that the microwires are single-crystalline and exhibit a long carrier lifetime, which is a good indication of a low defect density. Single-microwire photodetectors were fabricated as a prototype to showcase the potential of these microwires for optoelectronic applications. Thanks to the high carrier mobility of ~ 36 cm^2 V^{-1} s^{-1}, the photodetector shows a fast response with a short decay time of 295 μs. Moreover, the low defect density promises a device with a low noise current, which is crucial for the detection of weak light. The excellent responsivity and compact size render the single-microwire photodetector useful for the high-resolution spatial profiling of light intensity variations. As a preliminary demonstration, we built a setup for micro-feature detection based on the microwire detector and successfully resolved a 1 mm diameter thread. Notably, the lattice-framework synthesis process can also yield other single crystalline metal halide perovskites including $CsPbBr_3$ and $CH(NH_2)_2PbBr_3$ ($FAPbBr_3$) microwires. This novel strategy provides a flexible synthesis method for producing crystallization-kinetics-independent single-crystals, which may help to extend the application scope of halide perovskite materials and would be useful for engineering the shape of single-crystals in materials with intrinsic crystalline limitations.

Results and discussion

The synthesis of single-crystalline $CH_3NH_3PbBr_3$ microwires started with the fabrication of lead bromide ($PbBr_2$) microwires using a template-free antisolvent process, followed by a subsequent ion incorporation process to convert $PbBr_2$ into perovskite while maintaining the microwire architecture, as illustrated in Fig. 1a. The specific synthesis method is described in detail in the Experimental section. In brief, 1 mL of $PbBr_2$ in DMF (50 mg mL^{-1}) was added to a 5 mL vial, which was placed in a sealed antisolvent atmosphere (10 mL isopropanol in a 50 mL vial) at room temperature for 120 hours. The diffusion of antisolvent vapor into the small vial continuously lowered the solubility of $PbBr_2$ in DMF. Upon supersaturation, the $PbBr_2$ crystal seeds spontaneously nucleated and gradually evolved into self-assembled microwires. Interestingly, the dimensions of the $PbBr_2$ microwires depend strongly on the density of nucleation seeds, which can be controlled by the stirring rate of the supersaturated solution. Without stirring, $PbBr_2$ can grow into milliwires with diameters ranging from about 10 to 60 μm and lengths ranging from tens of microns to several centimeters (see Fig. S2, ESI†). When magnetic stirring was applied, the wire diameter and length drop significantly to less than 10 μm and 100 μm, respectively. The shrinkage in the dimensions is accompanied by a sharp increase in the wire density. Such observations can be attributed to the inhibition of the rapid crystallization on the $PbBr_2$ crystal seeds by stirring, thus allowing more wires with smaller dimensions to form during the growth process (see the schematic illustration in Fig. S1 for more details, ESI†). The obtained $PbBr_2$ microwires were then converted into $CH_3NH_3PbBr_3$ microwires by dipping them into a $CH_3NH_3Br_3$/isopropanol solution for 24 hours (see Fig. 1a for details), with the

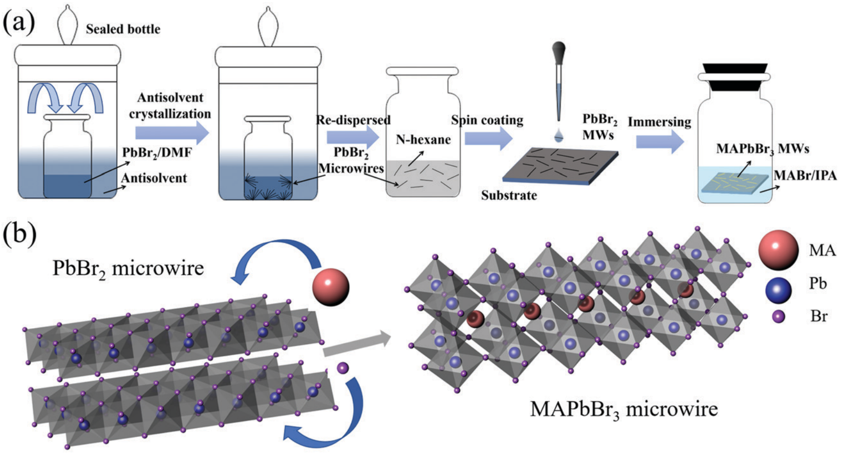

Fig. 1 (a) Schematic illustration of the antisolvent process for fabrication of $PbBr_2$ microwires and their conversion into perovskite microwires. (b) Schematic demonstration of converting the $PbBr_2$ crystal into the $CH_3NH_3PbBr_3$ perovskite structure by immersing the microwires into CH_3NH_3Br/isopropanol solution.

microwire dimensions being essentially unchanged during the conversion process. Notably, the $PbBr_2$ lattice framework can also be converted into other perovskites such as $CsPbBr_3$ and $FAPbBr_3$ by immersing the binary compound in the corresponding solution for ion diffusion (see Fig. S2 and S4 for more details, ESI†). Thus, using the two-step method outlined here, we can obtain $CH_3NH_3PbBr_3$ microwires with lengths tailorable from tens of microns to millimeters.

To understand how the conversion occurs, it is crucial to examine the crystal structures of $PbBr_2$ and $CH_3NH_3PbBr_3$. In both cases, each Pb^{2+} ion coordinates with six Br^- ions to form an octahedral ($PbBr_6^{4-}$) unit. During the solution supersaturated growth, the octahedral units are linked together *via* a combination of edge-connections and corner-connections,[34] as shown in Fig. 1b. The asymmetry in the crystal lattice gives rise to the anisotropic growth of $PbBr_2$ into a wire architecture. For cubic $CH_3NH_3PbBr_3$, the octahedral units are corner-connected in all three directions, with the $CH_3NH_3^+$ ions occupying the vertexes of the cubic lattice, thus forming a 3-dimensional framework. Hence, when dipping the $PbBr_2$ microwires into the CH_3NH_3Br/isopropanol solution, the $PbBr_6^{4-}$ octahedrons reconfigure into the perovskite framework in which the units all are corner-connected. At the same time, $CH_3NH_3^+$ and Br^- ions diffuse into the framework to complete the perovskite lattice structure, which is crucial for the luminescence properties of the crystal. According to theoretical calculations, the excitation and recombination processes occur within the octahedrons in which the Br 4p and Pb 6p orbitals contribute to the valence and conduction band edges, respectively.[35] A deficiency in Br would result in Br vacancy (V_{Br}) type defects, which form energy levels in the band gap and affect the recombination kinetics of the carriers.[36] Hence, it is crucial to use excess CH_3NH_3Br solution to provide enough $CH_3NH_3^+$ and Br^- ions in the conversion process to obtain perovskite microwires with intact crystal structures for fewer defect states and improved optoelectronic characteristics.

As a pioneer $PbBr_6^{4-}$-octahedron framework for perovskite, the crystal quality of the $PbBr_2$ microwires directly determines the optoelectronic properties of the converted perovskite microwires. Thus, it is of importance to realize high crystal quality $PbBr_2$ microwires. The scanning electron microscope (SEM) image of an ensemble of as-grown randomly scattered small $PbBr_2$ microwires is shown in Fig. 2a. Notably, other types of structures like micro-plates and randomly-shaped crystals are completely absent, revealing the excellent high yield of micro-wire structures. The microwires exhibit satisfactorily uniform diameters in the range of a few micrometers and show a well-defined square-shaped cross-section, as shown in the inset. Fig. 2b displays a large single $PbBr_2$ microwire with a diameter of about 30 μm. The extremely smooth surface is the first indication of its excellent crystal quality. Fig. 2c–e shows various typical single microwires obtained from the same run, which illustrate the growth uniformity of the structure with a preferred orientation along the longitudinal direction. It is worth noting that the black dots on the substrate show the residual solvent for dispersing the microwires. In addition, with a long enough growth time, the length of the $PbBr_2$ microwires can increase up to a centimeter, as shown in Fig. 2f. The large span in the dimensions of the $PbBr_2$ microwires indicates the flexibility of dimension control for the subsequent conversion into perovskite microwires. Using energy-dispersive X-ray spectroscopy (EDX), elemental mapping images were collected from the square dotted area of a typical $PbBr_2$ microwire as shown in Fig. 2g. The maps reveal that Pb and Br elements are evenly distributed over the entire area. In addition, the EDS spectrum yields an average Br/Pb ratio of 2.09, which is close to the stoichiometric ratio of $PbBr_2$. X-ray diffraction (XRD) was performed on single $PbBr_2$ microwires to further evaluate the crystal quality of the self-assembled structures. As shown in Fig. 2h, the characteristic diffraction peaks obtained from a single $PbBr_2$ microwire are sharp and almost equidistant, suggesting that the micro-structures are single-crystalline. Moreover, the XRD peaks can be attributed to diffraction from the (001) planes of the orthorhombic phase lead bromide crystal, similar to other reported works on lead iodide single-crystals.[37–39] Furthermore, the

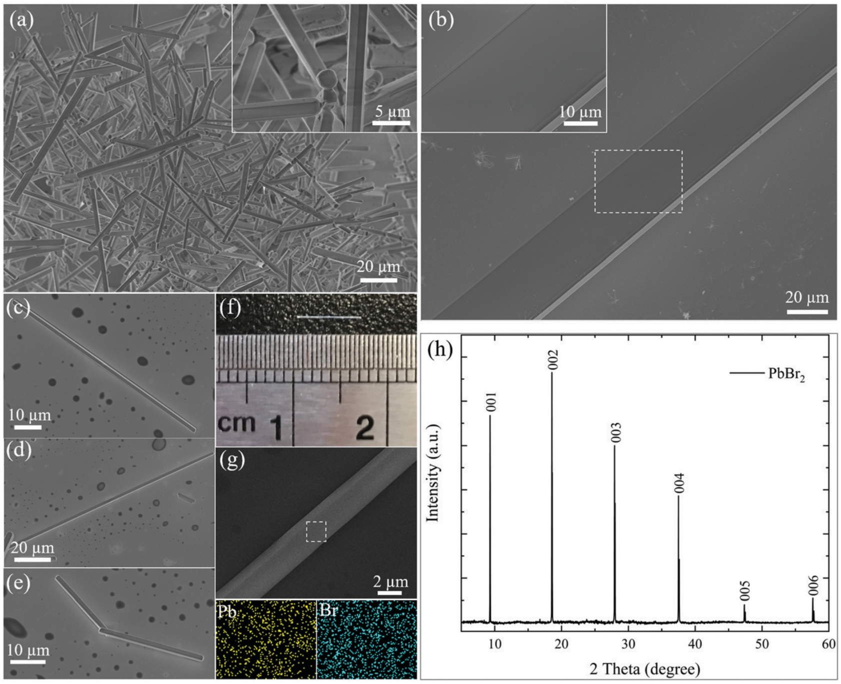

Fig. 2 (a) Top-view SEM image of an ensemble of randomly scattered $PbBr_2$ microwires; the inset is the enlarged image. (b) SEM images of a single $PbBr_2$ microwire with a particularly smooth surface. (c–e) SEM images of $PbBr_2$ microwires of different dimensions. (f) Optical image of a single large $PbBr_2$ microwire with a length approaching 1 cm. (g) Pb and Br elemental mapping images for the $PbBr_2$ microwire. (h) Corresponding XRD patterns of the single $PbBr_2$ microwire from (f).

specific value of the full width at half maximum (FWHM) of the 002 peak (excited by the Kα1 line) is as narrow as 0.038°, which shows the high crystal quality of $PbBr_2$. These exciting results prove that the as-assembled $PbBr_2$ microwires are single-crystals with a high crystalline quality, and these provide a perfect framework for the subsequent perovskite conversion.

The $PbBr_2$ microwires were then transformed into $CH_3NH_3PbBr_3$ microwires by introducing $CH_3NH_3^+$ and Br^- ions into the $PbBr_6^{4-}$ octahedron framework. Specifically, we immersed the $PbBr_2$ microwires into a CH_3NH_3Br/isopropanol solution. IPA was selected as the solvent because it can ionize CH_3NH_3Br without destroying the $PbBr_2$ crystalline structure. The converted $CH_3NH_3PbBr_3$ microwires exhibit a similar appearance to the starting $PbBr_2$ microwires (Fig. 3a and b). The lengths of these perovskite microwires can vary from 2 μm (inset of Fig. 3a) to 60 μm (Fig. 3b), which are within a similar range as the lengths of the $PbBr_2$ wires. The transformed $CH_3NH_3PbBr_3$ microwire displays an extremely smooth surface (the inset of Fig. 3b), which gives an initial indication of the excellent crystal quality of the obtained microwires. The optical images in Fig. S2 (ESI†) display the large-sized microwires before and after conversion. The dramatic color change from white in $PbBr_2$ to orange red in the $CH_3NH_3PbBr_3$ microwires can clearly be observed, indicating the completeness of the lattice transformation. Moreover, the high density of the microwires in Fig. S2 (ESI†) attests to the very high yield of this novel synthesis process. To confirm whether or not the $CH_3NH_3^+$ and Br^- ions have been effectively implanted into the $PbBr_2$ microwires, EDS elemental mapping images were collected from the microwire cross section. As seen in Fig. S3(c) (ESI†), C, Pb and Br are found to be evenly distributed over the entire area of interest. Furthermore, the quantitative elemental analysis yields an average Br/Pb ratio of 2.9, which is close to the stoichiometric ratio of the perovskite molecular formula. A series of XRD spectra taken at different dipping times were collected from a 60 μm-diameter single microwire to exhibit the change in lattice structure during the conversion process (see Fig. S5, ESI†). Once the $PbBr_2$ microwire had been immersed in the CH_3NH_3Br/IPA solution, the higher order diffraction peaks of $PbBr_2$ disappeared immediately, and the 001 and 002 peaks of $CH_3NH_3PbBr_3$ began to emerge. As the immersion time is increased, the diffraction peaks of $CH_3NH_3PbBr_3$ gradually grow stronger and dominate. At a long enough dipping time (>30 minutes), all of the $PbBr_2$ peaks had vanished, which implies that $PbBr_2$ had been completely converted into $CH_3NH_3PbBr_3$. The observations here clearly indicate the effective introduction of $CH_3NH_3^+$ and Br^- ions into the octahedron framework using this facile solution-based method, leading to the complete conversion of $PbBr_2$ into $CH_3NH_3PbBr_3$.

To further investigate the crystal quality of the obtained $CH_3NH_3PbBr_3$ microwires, we compare the XRD patterns obtained from a single microwire as well as a $CH_3NH_3PbBr_3$ single-crystal (detailed synthesis methods are described in the Experiment Section). As shown in Fig. 3c, the XRD peaks of the perovskite microwire are very consistent in position with those of the single-crystal, and can be perfectly indexed to the (001), (002) and (003) planes of the typical cubic-phase $CH_3NH_3PbBr_3$ perovskite crystal structure.[40] More importantly, the FWHM

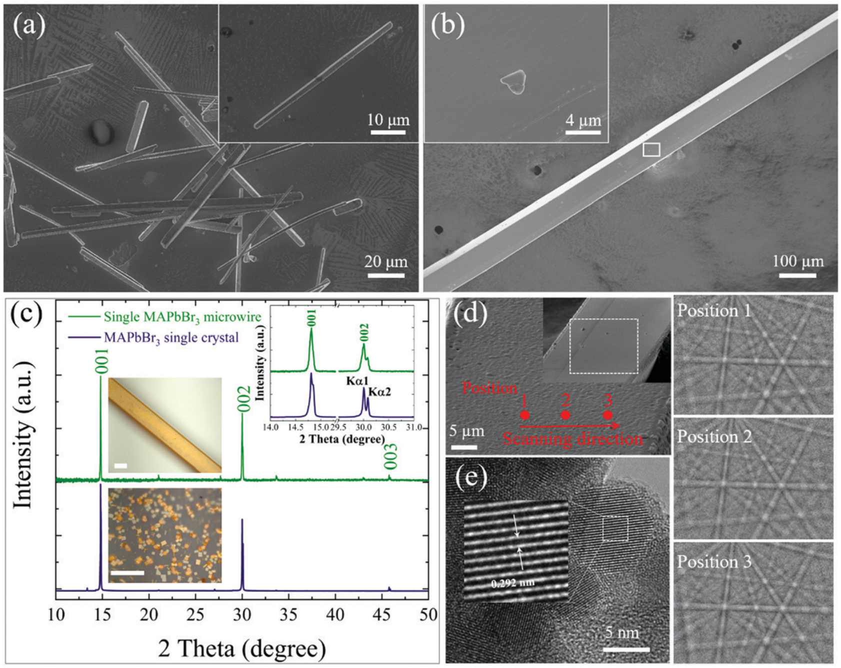

Fig. 3 (a) Top-view SEM images of various small $CH_3NH_3PbBr_3$ microwires randomly distributed on a substrate. Inset shows a single $CH_3NH_3PbBr_3$ microwire with a diameter of about 2 μm. (b) A large-dimension single $CH_3NH_3PbBr_3$ microwire with a diameter of about 60 μm, where the inset shows a magnified view of the boxed area showcasing the smooth surface of the converted $CH_3NH_3PbBr_3$ microwire. (c) Comparison of the XRD patterns obtained from a $CH_3NH_3PbBr_3$ microwire and a single-crystal. The inset shows a magnified view of the 001 and 002 peaks. Scale bars in optical images: 100 μm. (d) EBSD patterns obtained from three different positions (1–3) on a $CH_3NH_3PbBr_3$ microwire. The patterns are essentially identical, illustrating the single-crystal nature of the microwire. (e) HRTEM image of $CH_3NH_3PbBr_3$ microwires converted from $PbBr_2$ microwires.

values of the 001 and 002 peaks in our microwires are comparable with those in the single-crystal (Table S1, ESI†). These observations suggest that our microwires are actually single-crystalline. To further confirm this deduction, electron backscatter diffraction (EBSD) was applied. In this technique, the incident electron beam interacts with the surface of the material and generates an electron backscatter diagram, *i.e.* the Kikuchi patterns, by incoherent wide-angle electron scattering from the sample. By scanning the electron beam over a large area on the $CH_3NH_3PbBr_3$ microwire, we can study the crystalline coherency by observing the change in the Kikuchi patterns during the scan. Interestingly, the Kikuchi patterns (see Fig. 3d) are very clear and stable at different positions on the microwire, revealing the high crystal quality and long-range crystal lattice orientation consistency of the $CH_3NH_3PbBr_3$ microwire. This is further confirmed by a dynamic video in the ESI,† which shows that the Kikuchi pattern remains completely unchanged over an area of about 1125 μm^2. In this video, the acquisition time and accumulation of each pixel was set at 0.48 μs and 20 respectively, and 30 frames were acquired per second. Furthermore, high resolution transmission electron microscopy (HRTEM) was performed (Fig. 3e) to investigate the crystalline quality of the microwires. One can observe clear lattice fringes with a spacing of 0.292 nm, which corresponds to the (002) planes of the cubic $CH_3NH_3PbBr_3$ phase[41] These results clearly demonstrate that the transformed $CH_3NH_3PbBr_3$ microwires are single-crystalline, which has a significant impact on their optoelectronic properties.

To demonstrate the superior optoelectronic properties of our single-crystal $CH_3NH_3PbBr_3$ microwires, steady-state absorption, photoluminescence (PL) and time-resolved PL (TRPL) were implemented (Fig. 4). It can clearly be observed that the single $CH_3NH_3PbBr_3$ microwire emits bright green light under a 473 nm excitation (inset in Fig. 4a). The PL peak and absorption edge locate at ∼534 nm and ∼543 nm respectively (Fig. 4a), indicating again the successful conversion of the $CH_3NH_3PbBr_3$ microwire.[42] As shown in the fitting curves in Fig. 4a, the absorption spectrum shows a prominent band at about 522 nm and a broad absorption component, which could be respectively attributed to the excitonic absorption and continuum band absorption.[43] Moreover, we observed Fabry–Perot cavity like emission in the microwire in which light propagates along the microwire's longitudinal direction and bright green light is emitted in two ends. Such an emission pattern indicates the excellent cavity confinement of the well-faceted $CH_3NH_3PbBr_3$ microwires for potential applications in waveguide and even lasing action. In addition, the longer wavelength of the PL peak than the absorption edge can be attributed to the radiative recombination of the exciton. To estimate the carrier lifetimes, TRPL measurement was performed for investigating the carrier dynamics of an individual $CH_3NH_3PbBr_3$ microwire (Fig. 4b). The black circles represent the measured data for the PL decay, which were fitted using a bi-exponential profile (red line). The fitting curve shows a fast and a slow time component of $\tau_1 \approx 5.9$ ns and $\tau_2 \approx 98.8$ ns, respectively. The two different

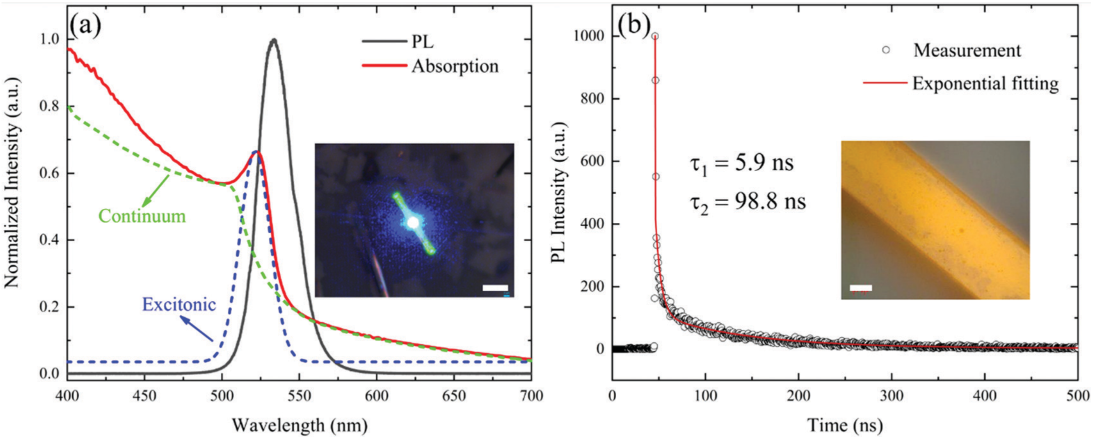

Fig. 4 (a) Absorption and PL spectra of $CH_3NH_3PbBr_3$ microwires under 473 nm excitation. The blue and green dashed lines represent the fitting curves of the absorption spectrum. The inset is the optical image of a light-emitting $CH_3NH_3PbBr_3$ microwire. Scale bar: 10 μm. (b) TRPL decay spectrum, with a bi-exponential fitting parameter of fast (5.9 ± 0.23 ns) and slow (98.8 ± 1.08 ns) transients. The inset shows the optical image of the microwire. Scale bar: 20 μm.

charge carrier lifetimes are associated with surface and bulk recombination, as in prior reports.[44] As a comparison, the carrier lifetime of the single-crystal synthesized *via* the one-step solution precipitation method was also performed (Fig. S6, ESI†) and the fast and slow time components were 3.7 ns and 97.4 ns, respectively. The carrier lifetimes of the $CH_3NH_3PbBr_3$ microwires are comparable with those of the $CH_3NH_3PbBr_3$ single-crystal, which indirectly indicates once again that our microwires are single-crystalline. The above crystal structure and material characterizations demonstrate the excellent optical properties of the perovskite microwires, which contribute to the realization of high performance optoelectronic devices.

To demonstrate the potential of the single-crystal microwires for optoelectronic applications, metal–semiconductor–metal (MSM) photodetectors were fabricated based on individual $CH_3NH_3PbBr_3$ microwires and the schematic of the device is shown in Fig. 5a. Gold electrodes of around 300 nm thickness were evaporated on the two ends of the single microwire. With the microwire diameter being 40 μm and the space between the two electrodes being about 100 μm (shown in the Fig. S8, ESI†), the active area for light detection is estimated to be about 4000 μm^2. The current–voltage (*I–V*) curves of the photodetector measured in the dark and under the illumination of a 450 nm laser with different intensities are all linear, indicating that the contacts are ohmic and that the device works as a photoconductive detector (Fig. 5b). In particular, the photocurrent increases linearly from 0.1 nA to 374.9 nA when the irradiation power is increased from 0.8 nW to 19.5 μW, as shown in the inset of Fig. 5b. This linear dependence gives rise to a linear dynamic range (LDR) of at least 88 dB, where the details of the calculations can be found in the ESI.† Such a respectably wide LDR reveals that our microwire photodetectors can be useful for practical optical communication and imaging applications.

In addition to the capability of detecting light with a wide range of intensities, the temporal response is also an important indicator of the performance of a photodetector. Fig. 5c displays the response of the photocurrent under alternating optical switching at a frequency of 0.5 Hz. The device exhibits a high on/off ratio of $\sim 8.8 \times 10^3$ when biased at 5 V, under an illumination power of 19.5 μW. Moreover, the dynamic photoresponse is very stable under continuous optical switching without any observable hysteresis or degradation in the on/off ratio. When the bias voltage decreases, the same stable switching behavior is observed while the photocurrent drops accordingly (see Fig. S8, ESI†). Such a repeatable smooth switching can be attributed to the very low density of trap states inside the single-crystal and at the MS-interface. Fig. 5d illustrates the temporal responses of the photodetector switching between on and off states, using a 450 nm laser modulated at 20 Hz. The rise and fall times are measured to be 113 μs and 295 μs, respectively, which compare favorably with the transition times of other similar microwire photodetectors.[45,46] The fast response can be attributed to the high carrier mobility of 36 $cm^2 V^{-1} s^{-1}$, which is close to that of the bulk single-crystal[6] (see Fig. S7 for details, ESI†). The fast and stable switching behavior observed renders our microwire photodetector potentially useful for high-speed light detection, which is crucial for modern optical communications.

To evaluate the capability of the microwire photodetector for weak light detection, responsivity (*R*) curves were measured under different biasing voltages, as shown in Fig. 5e. Details of the measurement can be found in the ESI.† In general, the three curves exhibit similar dependences on the wavelength of the incident light, with the responsivity increasing with the biasing voltage. The device shows a decent light response from 300 nm to more than 550 nm, covering the near-UV and most of the visible light regions. In particular, under a 5 V bias, the responsivity reaches a maximum value of 0.1 A W^{-1} at 530 nm and drops quickly at longer wavelengths. Such a rapid decay is consistent with the absorption spectrum in Fig. 4a, which reveals that the absorption edge (and thus the bandgap) of single-crystal $MAPbBr_3$ is located at around 540 nm. Noise is the basic limitation for the detection of weak light in photodetectors. As seen in Fig. 5f, the noise current is as low as 3.8×10^{-13} A $Hz^{-1/2}$ at 70 Hz under a bias of 5 V and is almost

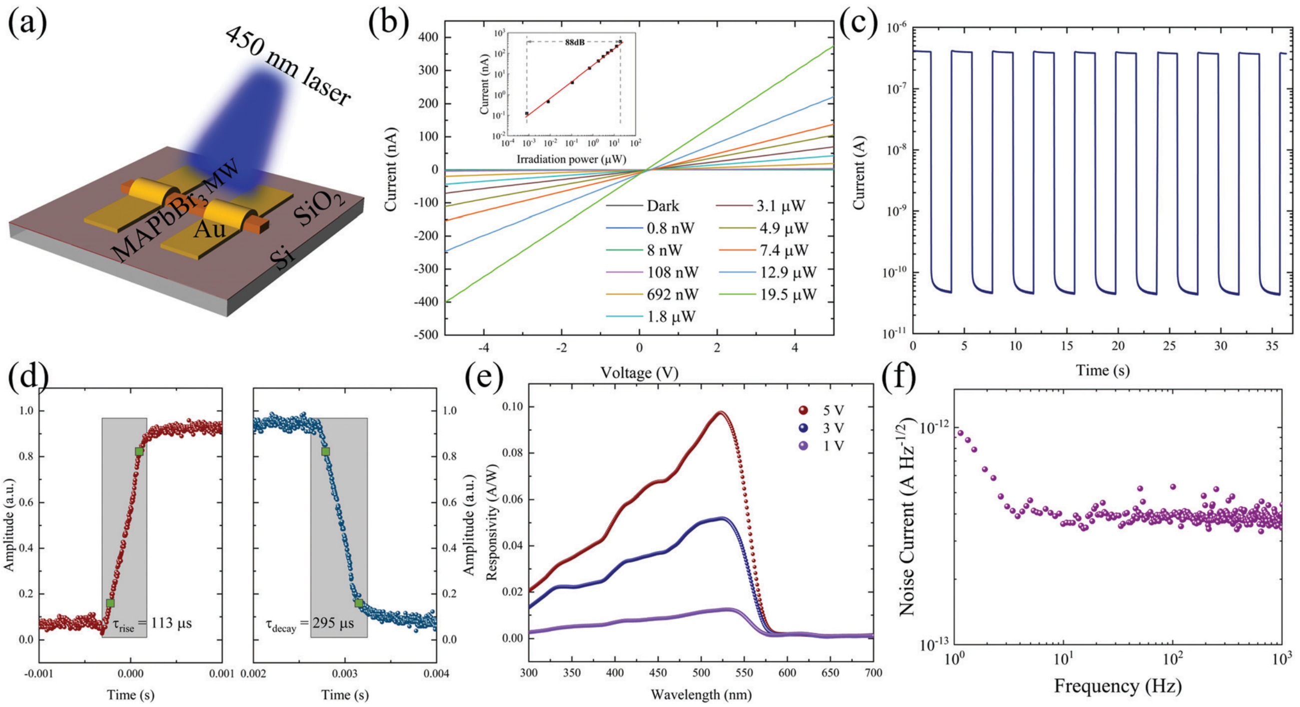

Fig. 5 (a) Schematic of the single $CH_3NH_3PbBr_3$ microwire-based photodetector. (b) *I–V* curves of the device measured at room temperature under dark and illumination with 450 nm light of different power levels; the inset shows the linear dynamic range of the photodetector under 5 V. (c) Photocurrent variation under continuous switching between dark and bright (irradiation power = 19.5 μW) conditions. (d) Transient response of the device. The rise and fall times are well below 300 μs. (e) Responsivity of the photodetector under different bias voltages. (f) The noise current of the photodetector measured at a bias voltage of 5 V. At low frequencies, the noise current is at the 0.1 pA level, attesting to the low defect density of the microwire.

constant over the frequency range of $10–10^3$ Hz. We note that such a low noise current in the low frequency region compares favorably with some of the best perovskite-based photodetectors reported in the literature.[47,48] In the low frequency range, the noise current is essentially dominated by the flicker noise, which originates from the electronic transitions involving trap/defect states. The low noise current observed in the low-frequency region indicates that the defect density in our perovskite microwires is extremely low, which once again attests to the excellent crystal quality of the single-crystal micro-structure. Based on the noise current and the responsivity, the specific detectivity (D^*) is estimated according to the following equations.

$$D^* = \frac{\sqrt{AB}}{\mathrm{NEP}} \quad \mathrm{NEP} = \frac{i_n}{R}$$

where A is the active area, B is the bandwidth, i_n is the noise current and the NEP is the noise equivalent power. As shown in Fig. S9 in the ESI,† D^* reaches a maximum value of 1.4×10^9 cm $\mathrm{Hz^{1/2}\ W^{-1}}$ at 530 nm, which is a reasonably good number for a single microwire photodetector with a lateral device architecture and a relatively small light detection area. The exciting results here fully demonstrate that our single-crystal perovskite microwires, possessing a very low defect density, can be useful for photodetection and other optoelectronic applications that require a fast response, high optical sensitivity and low background noise.

In addition to the low noise current being useful for the detection of weak light, the small size of the microwire enables its application potential in pixel enhancement for imaging and the detection of small objects. As a proof of concept, we established a micro-object detection system (MODS) based on our single microwire photodetector and achieved a spatial resolution of around 1 mm in one dimension. Fig. 6a shows the schematic diagram of the MODS, which consists of a white point light source with adjustable optical power, a quartz glass plate sample holder (6 cm below the light source), and a single crystal microwire detector placed on top of a one-dimensional sliding stage. During the measurement, the microwire detector moved at a speed of 50 mm $\mathrm{min^{-1}}$ along the horizontal direction under the transparent sample holder and the spacing between them is about 1 mm. Owing to the miniature size of the microwire, our photodetector is capable of detecting the local light intensity variation with sub-millimeter precision over the entire scanning range in space. The output current of the photodetector was recorded continuously using a computer-controlled Keithley 2601 with the device biased at +15 V. Fig. S10(d and e) (ESI†) shows the one-dimensional photocurrent (and thus light intensity) profiles of the point light source operating at different power levels, over a scanning range of 100 mm. All profiles assume a Gaussian distribution but with some deviations in the central region, possibly due to the focusing optics present in the light source. Such a capability of measuring the spatial light intensity profiles with high precision

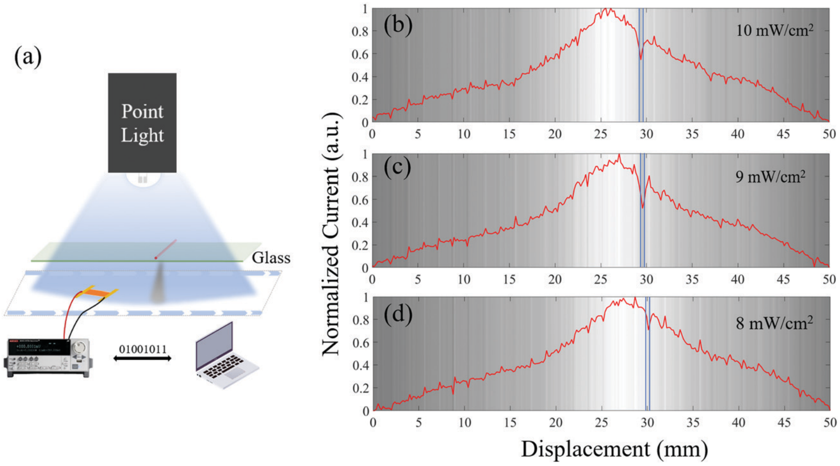

Fig. 6 (a) Schematic of the micro-object detection system. A 1 mm thread is placed on the glass sample holder to induce a local light intensity fluctuation which can be detected precisely by the moving single-wire detector underneath. (b–d) Normalized photocurrent spatial profiles obtained under different light intensities. The obvious dip at around 30 mm clearly indicates the position of the 1 mm thread.

is useful for micro-feature detection. To demonstrate such potential, we placed on the sample holder a 1 mm opaque fine thread whose orientation is perpendicular to the motion of the microwire photodetector (see the illustration in Fig. 6a). Fig. 6b–d, displays the photocurrent profiles in the presence of the fine thread under different light intensities. The colored stripes in the background of the line profiles are a grayscale representation of the photocurrent detected at that particular location. When the light intensity exceeds 8 mW cm^{-2}, an obvious dip can be observed at around 30 mm (*i.e.* when the microwire photodetector is 30 mm away from the starting point), indicating the position at which the fine thread partially blocks the light. From the width of the dip, we can calculate the diameter of the object to be in the range of 0.8–1.4 mm, which is within an acceptable error range of its actual size. Moreover, we have established a visible light communication system with the perovskite microwire and obtained a remarkably stable and accurate transmission and reception of signals between a blue light-emitting diode and the microwire photodetector (see Fig. S11 for detailed information, ESI†). These demonstrations clearly reveal that these compact single-crystalline microwires with excellent optoelectronic properties can potentially be integrated into a full system for a wide range of practical applications in imaging, inspection and other fields.

Conclusions

In summary, we have developed a novel strategy to produce single-crystal halide perovskite microwires *via* the efficient incorporation of organic monovalent ions into the $PbBr_2$ lattice framework. Owing to the anisotropic crystal lattice, $PbBr_2$ could be grown spontaneously into self-assembled microwires with lengths ranging from microns to centimeters at room temperature using an optimized anti-solvent method. By incorporating the organic monovalent ions into the $PbBr_2$ lattice framework, we have successfully demonstrated the synthesis of single-crystal organic–inorganic hybrid $CH_3NH_3PbBr_3$ microwires. In particular, the long carrier lifetime of over 100 ns and high carrier mobility of ~36 $cm^2\ V^{-1}\ s^{-1}$ clearly indicate the low density of defects in the microwire. Single-microwire photodetectors were fabricated to showcase their potential for optoelectronic applications. High photoresponsivity, a fast response time (<295 μs) and an ultra low noise current render the microwire detector useful for weak light detection at high speed, which is crucial for modern optical communications. In addition, the compact size of the single-wire detector enables light intensity profiling with high spatial resolution. In particular, we achieved a spatial resolution of 1 mm, using a micro-object detection system based on the single-wire detector. The exciting results in this work not only provide a novel route for acquiring high quality perovskite microwires which can be applied in micro optoelectronic devices, but also put forward a new growth mechanism that is not affected by the original crystal phase of perovskite, thus breaking the limit for perovskite, and which may lead to variable structures that can satisfy different optoelectronic demands.

Experimental section

Chemicals

Lead bromide ($PbBr_2$, 99.99%), methylamine bromide (CH_3NH_3Br, 99.5%) and formamidinium bromide ($CH(NH_2)_2Br$, 99.5%) were purchased from Xi'an Polymer Light Technology Corp. Cesium bromide (CsBr, 99.9%) was purchased from Alfa Aesar. *N*,*N*-Dimethylmethanamide (DMF, 99.5%), and isopropyl alcohol (IPA, 99.7%) were purchased from Sinopharm Chemical Reagent Co., Ltd. N-Hexane (99.0%) was purchased from Shanghai Aladdin Biochemical Technology Co., Ltd. Dichloromethane (CH_2Cl_2, 99.9%) was purchased from Acros Organics. All chemicals were used without any further purification.

Preparation of $PbBr_2$ microwires

$PbBr_2$ microwires were synthesized using the improved anti-solvent method. 50 mg pure $PbBr_2$ powder was completely dissolved in 1 mL DMF solution with 1 hour of thermal heating at 90 °C. The above solution was then added into a 5 mL vial, which was placed in a sealed antisolvent atmosphere (10 mL IPA in a 50 mL vial) at room temperature. The $PbBr_2$ microwires were crystallized within a period of 3 days. The obtained $PbBr_2$ microwires were rinsed with 3 mL N-hexane to remove the mixture solvent of IPA and DMF in the small vial. The obtained $PbBr_2$ microwires had a diameter of about 10–60 μm and were dried in a nitrogen atmosphere. To obtain small diameter (1–10 μm) $PbBr_2$ microwires, a magneton was added to the small vial and the antisolvent setup was placed on a magnetic stirrer at a rotation rate of 180 rpm. The other experimental conditions were the same as above and the small dimension $PbBr_2$ microwires were re-dispersed in 5 mL N-hexane after rinsing with N-hexane.

Synthesis of perovskite microwires

The CH_3NH_3Br, $CH(NH_2)_2Br$ and CsBr powder was completely dissolved in isopropanol solution with 1 hour of thermal heating at 90 °C to obtain concentrations of 20 mg mL^{-1}, 20 mg mL^{-1} and 5 mg mL^{-1}, respectively. Then the $PbBr_2$ microwires in N-hexane were dispersed onto a glass substrate by spin coating with a rotating speed of 1000 rpm min^{-1} for 30 s before being immersed in the above solutions overnight. In addition, a longer soaking time will result in a more complete conversion. All conversion processes were performed thoroughly under a nitrogen atmosphere and all the perovskite microwires samples were rinsed in IPA first and then the residual solvent removed with N-hexane before use.

Synthesis of $CH_3NH_3PbBr_3$ single-crystal

The $CH_3NH_3PbBr_3$ perovskite single-crystals were synthesized using a common one-step antisolvent solution saturation crystallization method. In short, 73.4 mg $PbBr_2$ and 22.4 mg CH_3NH_3Br were completely dissolved in 1 mL DMF to form a $CH_3NH_3Br{\cdot}PbBr_2$ solution (0.2 M). Then 10 μL of the prepared solution was added dropwise onto a 1.5 × 1.5 cm glass substrate, which was placed in a sealed antisolvent atmosphere (10 mL dichloromethane in a 50 mL vial) at room temperature. It is worth noting that the glass substrate is above the liquid surface. After 24 hours, the antisolvent vapor diffused into the $CH_3NH_3Br{\cdot}PbBr_2$ droplet and $CH_3NH_3PbBr_3$ perovskite single-crystals were crystallized on the substrate.

Device fabrication

A single $CH_3NH_3PbBr_3$ microwire was picked out and placed on a 1 × 1 cm^2 silicon oxide substrate. Gold electrodes were evaporated with a hard mask placed on the surface of the microwire in the vacuum evaporation machines. The hard mask was made with a laboratory laser marking machine and the effective occlusion area was 2 × 0.1 mm^2. With a relatively slow evaporation rate ($\sim$0.3 Å s^{-1}) of gold, the thickness of the final vapor deposition on the surface of the microwire is about 300 nm. Finally, the active area of the photodetector was about 4000 μm^2 as defined by the area of the microwire not covered by the electrodes.

Material characterizations

The optical images of all microwires were captured using a Zeiss AxioCam ICc 5 microscope. The steady-PL of the halide perovskite samples was monitored using a Confocal Laser Raman Spectrometer (LabRAM HR Evolution, HORIBA, Japan) with a 473 nm excitation laser. The absorption spectrum of the as-prepared samples was measured using a UV-vis spectrophotometer (UV-2600, Shimadzu, Japan). The XRD measurements were carried out with a Rigaku Smart Lab 9kW system rotating anode X-ray source with Cu ($\lambda \approx 1.54$ Å) coupling with the high-quality semiconductor detector, and a step size of 0.002 degree. The scanning electron microscopy (SEM) images were obtained using a Zeiss Sigma with a Schottky Field Emission source operating at 2 kV. Energy-disperse X-ray spectroscopy (EDX) data were collected from the samples using the same SEM embedded EDX detector at an operating voltage of 20 kV. The Kikuchi lines were obtained using the technique of Electron Backscatter Diffraction (EBSD) on a Zeiss Crossbeam 540 Gemini 2 operating at a 10 kV accelerating voltage and a 3 nA acquisition current. The fluorescence lifetime decay was recorded by Time Correlated Single Photon Counting (TCSPC) using an Edinburgh FS5 fluorescence spectrophotometer with a picosecond laser of 405 nm at room temperature. The HRTEM measurements were carried out on a Talos F200X, FEI operating at 200 kV. The *I–V* curves and optical switching *I–t* measurements were performed using a semiconductor device analyzer (KEYSIGHT B1500A) equipped with a SEMISHARE probe station. The response speed was measured with a Tektronix MDO4054C Mixed Domain Oscilloscope cooperated with a low-noise current preamplifier SR570 (Stanford Research Systems) and the optical switch of the laser source was controlled using a RIGOL DG4602 Function/Arbitrary Waveform Generator. The responsivity of the device with different monochromatic light wavelengths was obtained from a photodetection spectral response calibration system (Zolix Instruments). The noise current curves of the device were obtained using the ProPlus 9812D wafer-level 1/*f* noise characterization system.

Author contributions

S. S. Y. synthesized the material and performed the device fabrication, characterization, and analysis with help from S. P. W. X. H. X., Y. C. K., Y. M., J. Z. J. and L. S. performed the device characterization, design and carried out the demonstrations. S. C. S. and Z. K. T. interpreted the results. All authors discussed the results and prepared the manuscript. S. P. W. and K. W. N. supervised the work.

Conflicts of interest

There are no conflicts to declare.

Acknowledgements

This work was funded by the Science and Technology Development Fund, Macau SAR (File no. 199/2017/A3, 0038/2019/A1, 0125/2018/A3 and 0071/2019/AMJ), Multi-Year Research Grants (MYRG2017-00149-FST, MYRG2018-00086-IAPME, and MYRG2017-00152-FST) from the University of Macau, Guangdong Province International Scientific and Technological Cooperation Project (Grant No. 2020A0505100011), Scientific and Technological Plan of Guangdong Province, China (Grant No. 2019B090905005) and the Natural Science Foundation of Heilongjiang Province (No. QC2017077).

References

1 C. Bi, Y. Yuan, Y. Fang and J. Huang, *Adv. Energy Mater.*, 2015, **5**, 1401616.
2 Q. Dong, Y. Fang, Y. Shao, P. Mulligan, J. Qiu, L. Cao and J. Huang, *Science*, 2015, **347**, 967–970.
3 S. Draguta, S. Thakur, Y. V. Morozov, Y. Wang, J. S. Manser, P. V. Kamat and M. Kuno, *J. Phys. Chem. Lett.*, 2016, **7**, 715–721.
4 K. Lin, J. Xing, L. N. Quan, F. P. G. de Arquer, X. Gong, J. Lu, L. Xie, W. Zhao, D. Zhang and C. Yan, *Nature*, 2018, **562**, 245–248.
5 L. Mao, Y. Wu, C. C. Stoumpos, B. Traore, C. Katan, J. Even, M. R. Wasielewski and M. G. Kanatzidis, *J. Am. Chem. Soc.*, 2017, **139**, 11956–11963.
6 D. Shi, V. Adinolfi, R. Comin, M. Yuan, E. Alarousu, A. Buin, Y. Chen, S. Hoogland, A. Rothenberger and K. Katsiev, *Science*, 2015, **347**, 519–522.
7 T. C. Sum and N. Mathews, *Energy Environ. Sci.*, 2014, **7**, 2518–2534.
8 W. Deng, X. Zhang, L. Huang, X. Xu, L. Wang, J. Wang, Q. Shang, S. T. Lee and J. Jie, *Adv. Mater.*, 2016, **28**, 2201–2208.
9 A. Kojima, K. Teshima, Y. Shirai and T. Miyasaka, *J. Am. Chem. Soc.*, 2009, **131**, 6050–6051.
10 N. J. Jeon, H. Na, E. H. Jung, T.-Y. Yang, Y. G. Lee, G. Kim, H.-W. Shin, S. I. Seok, J. Lee and J. Seo, *Nat. Energy*, 2018, **3**, 682–689.
11 X. Y. Chin, D. Cortecchia, J. Yin, A. Bruno and C. Soci, *Nat. Commun.*, 2015, **6**, 7383.
12 S. P. Senanayak, B. Yang, T. H. Thomas, N. Giesbrecht, W. Huang, E. Gann, B. Nair, K. Goedel, S. Guha and X. Moya, *Sci. Adv.*, 2017, **3**, e1601935.
13 Z. Xiao, R. A. Kerner, L. Zhao, N. L. Tran, K. M. Lee, T.-W. Koh, G. D. Scholes and B. P. Rand, *Nat. Photonics*, 2017, **11**, 108–115.
14 Z.-K. Tan, R. S. Moghaddam, M. L. Lai, P. Docampo, R. Higler, F. Deschler, M. Price, A. Sadhanala, L. M. Pazos and D. Credgington, *Nat. Nanotechnol.*, 2014, **9**, 687–692.
15 G. Maculan, A. D. Sheikh, A. L. Abdelhady, M. I. Saidaminov, M. A. Haque, B. Murali, E. Alarousu, O. F. Mohammed, T. Wu and O. M. Bakr, *J. Phys. Chem. Lett.*, 2015, **6**, 3781–3786.
16 L. Li, H. Chen, Z. Fang, X. Meng, C. Zuo, M. Lv, Y. Tian, Y. Fang, Z. Xiao and C. Shan, *Adv. Mater.*, 2020, 1907257.
17 X. Yang, J. Wu, T. Liu and R. Zhu, *Small Methods*, 2018, **2**, 1800110.
18 W. Zhang, L. Peng, J. Liu, A. Tang, J. S. Hu, J. Yao and Y. S. Zhao, *Adv. Mater.*, 2016, **28**, 4040–4046.
19 Y. Gao, S. Wang, C. Huang, N. Yi, K. Wang, S. Xiao and Q. Song, *Sci. Rep.*, 2017, **7**, 45391.
20 M. Jiang, W. Mao, X. Zhou, C. Kan and D. Shi, *ACS Appl. Mater. Interfaces*, 2019, **11**, 11800–11811.
21 I. Dursun, Y. Zheng, T. Guo, M. De Bastiani, B. Turedi, L. Sinatra, M. A. Haque, B. Sun, A. A. Zhumekenov and M. I. Saidaminov, *ACS Energy Lett.*, 2018, **3**, 1492–1498.
22 Z. Gu, W. Sun, K. Wang, N. Zhang, C. Zhang, Q. Lyu, J. Li, S. Xiao and Q. Song, *J. Mater. Chem. A*, 2016, **4**, 8015–8019.
23 C. Wehrenfennig, G. E. Eperon, M. B. Johnston, H. J. Snaith and L. M. Herz, *Adv. Mater.*, 2014, **26**, 1584–1589.
24 Z. Gu, K. Wang, W. Sun, J. Li, S. Liu, Q. Song and S. Xiao, *Adv. Opt. Mater.*, 2016, **4**, 472–479.
25 H. Gao, J. Feng, Y. Pi, Z. Zhou, B. Zhang, Y. Wu, X. Wang, X. Jiang and L. Jiang, *Adv. Funct. Mater.*, 2018, **28**, 1804349.
26 S. X. Li, Y. S. Xu, C. L. Li, Q. Guo, G. Wang, H. Xia, H. H. Fang, L. Shen and H. B. Sun, *Adv. Mater.*, 2020, 2001998.
27 P. Liu, X. He, J. Ren, Q. Liao, J. Yao and H. Fu, *ACS Nano*, 2017, **11**, 5766–5773.
28 J. Feng, C. Gong, H. Gao, W. Wen, Y. Gong, X. Jiang, B. Zhang, Y. Wu, Y. Wu, H. Fu, L. Jiang and X. Zhang, *Nat. Electron.*, 2018, **1**, 404–410.
29 W. Deng, L. Huang, X. Xu, X. Zhang, X. Jin, S. T. Lee and J. Jie, *Nano Lett.*, 2017, **17**, 2482–2489.
30 S.-X. Li, G.-P. Zhang, H. Xia, Y.-S. Xu, C. Lv and H.-B. Sun, *Nanoscale*, 2019, **11**, 18272–18281.
31 Z. Wang, J. Liu, Z.-Q. Xu, Y. Xue, L. Jiang, J. Song, F. Huang, Y. Wang, Y. L. Zhong and Y. Zhang, *Nanoscale*, 2016, **8**, 6258–6264.
32 F. Chen, C. Xu, Q. Xu, Y. Zhu, F. Qin, W. Zhang, Z. Zhu, W. Liu and Z. Shi, *ACS Appl. Mater. Interfaces*, 2018, **10**, 25763–25769.
33 Y.-X. Chen, Q.-Q. Ge, Y. Shi, J. Liu, D.-J. Xue, J.-Y. Ma, J. Ding, H.-J. Yan, J.-S. Hu and L.-J. Wan, *J. Am. Chem. Soc.*, 2016, **138**, 16196–16199.
34 Z. Yuan, C. Zhou, Y. Tian, Y. Shu, J. Messier, J. C. Wang, L. J. Van De Burgt, K. Kountouriotis, Y. Xin and E. Holt, *Nat. Commun.*, 2017, **8**, 14051.
35 V. K. Ravi, G. B. Markad and A. Nag, *ACS Energy Lett.*, 2016, **1**, 665–671.
36 Y. Liu, K. Palotas, X. Yuan, T. Hou, H. Lin, Y. Li and S.-T. Lee, *ACS Nano*, 2017, **11**, 2060–2065.
37 J. Verwey and J. Schoonman, *Physica*, 1967, **35**, 386–394.
38 Y. He, S. Zhu, B. Zhao, Y. Jin, Z. He and B. Chen, *J. Cryst. Growth*, 2007, **300**, 448–451.
39 Z. Zheng, A. Liu, S. Wang, Y. Wang, Z. Li, W. M. Lau and L. Zhang, *J. Mater. Chem.*, 2005, **15**, 4555–4559.
40 M. I. Saidaminov, A. L. Abdelhady, B. Murali, E. Alarousu, V. M. Burlakov, W. Peng, I. Dursun, L. Wang, Y. He and G. Maculan, *Nat. Commun.*, 2015, **6**, 1–6.
41 L. C. Schmidt, A. Pertegás, S. González-Carrero, O. Malinkiewicz, S. Agouram, G. Minguez Espallargas, H. J. Bolink, R. E. Galian and J. Pérez-Prieto, *J. Am. Chem. Soc.*, 2014, **136**, 850–853.
42 M. Zhang, H. Yu, M. Lyu, Q. Wang, J.-H. Yun and L. Wang, *Chem. Commun.*, 2014, **50**, 11727–11730.

43 Y. Yang, Y. Yan, M. Yang, S. Choi, K. Zhu, J. M. Luther and M. C. Beard, *Nat. Commun.*, 2015, **6**, 1–6.

44 M. I. Saidaminov, V. Adinolfi, R. Comin, A. L. Abdelhady, W. Peng, I. Dursun, M. Yuan, S. Hoogland, E. H. Sargent and O. M. Bakr, *Nat. Commun.*, 2015, **6**, 1–7.

45 P. Gui, Z. Chen, B. Li, F. Yao, X. Zheng, Q. Lin and G. Fang, *ACS Photonics*, 2018, **5**, 2113–2119.

46 X. Mo, X. Li, G. Dai, P. He, J. Sun, H. Huang and J. Yang, *Nanoscale*, 2019, **11**, 21386–21393.

47 J. Feng, C. Gong, H. Gao, W. Wen, Y. Gong, X. Jiang, B. Zhang, Y. Wu, Y. Wu and H. Fu, *Nat. Electron.*, 2018, **1**, 404–410.

48 L. Dou, Y. M. Yang, J. You, Z. Hong, W.-H. Chang, G. Li and Y. Yang, *Nat. Commun.*, 2014, **5**, 1–6.